Static and dynamic fluid-driven fracturing of adhered elastica

Thomasina V. Ball*

BP Institute, Department of Earth Sciences,

University of Cambridge, Bullard Laboratories,

Madingley Road, Cambridge, CB3 0EZ, United Kingdom

Jerome A. Neufeld

BP Institute, Department of Earth Sciences,

Department of Applied Mathematics and Theoretical Physics,

University of Cambridge, Bullard Laboratories,

Madingley Road, Cambridge, CB3 0EZ, United Kingdom

(Dated: November 29, 2017)

Abstract

The transient spreading of a viscous fluid beneath an elastic sheet adhered to the substrate is controlled by the dynamics at the tip where the divergence of viscous stresses necessitates the formation of a vapour tip separating the fluid front and fracture front. A simple theoretical model is developed showing that adhesion gives rise to the possibility of static, elastic droplets and to two dynamical regimes of spreading; viscosity dominant spreading controlled by flow of fluid into the vapour tip, and adhesion dominant spreading. Constant flux experiments using clear, PDMS elastic sheets enable new, direct measurements of the vapour tip, and confirm the existence of viscosity and adhesion dominant spreading regimes. The theory and experiments thereby provide an important test coupling the dynamics of flow with elastic deformation with important implications in fluid-driven fracturing of elastic media more generally.

* tvb21@cam.ac.uk

I. INTRODUCTION

The geometry and propagation of fluid-driven fractures is determined by a competition between the flow of viscous fluid, the elastic deformation of the solid and the energy required to create new surfaces. These processes feature industrially in the hydraulic fracturing of shale [1], but are also commonplace in nature, from magmatic intrusions in the Earth's crust [2, 3], to the propagation of cracks at the base of glaciers [4]. The relationship between elastic deformation and adhesion energy has been successfuly considered for the development of stretchable electronics made from buckled nanoribbons [5, 6]. Similarly, the coupling of viscous spreading and elastic deformation has been analysed when looking at the dynamics of blisters spreading over a pre-wetted film [7] with applications to the flow of biofluids through deformable vessels [8] and the suppression of viscous fingering in an elastic-walled Hele-Shaw cell [9]. However, the physical processes underlying the dynamics of the fluid-driven fracturing of thin adhered elastica remain unexplored and unobserved.

The transient spreading of a viscous fluid beneath an adhered elastic sheet is controlled by the dynamics at the tip. The centrality of the physics at the contact line is directly analogous to the capillary-driven spreading of a droplet, where elasticity plays the role of surface tension. Near the front, a large negative pressure gradient is needed to drive the viscous fluid into the narrowing gap of the fracture where the rate of viscous dissipation diverges. This is the elastic equivalent of Huh and Scriven's paradox [10], and theoretically leads to an immobile contact line. In the context of a spreading droplet, microscopic mechanisms such as a precursor film [11] and relaxation of the no-slip conditions at the front [10] have been proposed to account for experimental observations. For the problem of a viscous fluid spreading underneath an elastic sheet, a macroscopic precursor film has been used to regularise this contact-line singularity [7], but this fails to explain fracturing phenomena, such as magmatic intrusions, where there is no evidence of a pre-wetted surface.

We show through consideration of a simple lubrication model that a fluid lag, or vapour tip, develops between the fluid front and the fracture front, Fig. 1. Importantly we also demonstrate an observational system capable of characterising the vapour tip, thereby confirming the presence of a vapour tip and its role in the transient dynamics. The addition of a fluid lag regularises the contact line by imposing a finite fluid thickness at the fluid front [12]. A fluid lag has previously been invoked in other contexts, when modelling penny-

shaped cracks [13] and buoyancy-driven fractures [14], and has been observed in laboratory experiments on the fracturing of elastic blocks [15–17] but has not been systematically characterised. Our development of a theoretical model and consistent laboratory experiments using thin elastica lead to a simpler analysis and treatment of fluid-driven fracturing and provides a usefully reduced system in which to understand the dynamics of fluid-driven fracturing, with direct biological and manufacturing implications.

To delaminate adhered elastica, the energy required to create new surfaces is $\Delta\gamma = \gamma_{SV}^{(\text{sheet})} + \gamma_{SV}^{(\text{substrate})} - \gamma_{SS}$, where γ_{SV} is the solid-vapour surface energy and γ_{SS} the solid-solid surface energy. This imposes a curvature at the fracture front, or fracture criterion, given by

$$\kappa = \sqrt{2}/l_{ec}, \quad \text{where} \quad l_{ec} = (B/\Delta\gamma)^{1/2}, \tag{1}$$

the elastocapillary lengthscale, with bending stiffness B [18]. The material strength of adhesion allows for the possibility of static solutions, and controls the long-time behaviour of spreading.

We show that two dynamical regimes are possible; viscosity dominant spreading controlled by the pressure gradient driving fluid into the vapour tip and adhesion dominant spreading controlled by interfacial adhesion. These two regimes are analogous to the limiting regimes of propagation for a semi-infinite hydraulic crack in an elastic medium [13]. In the elastic bending case considered here, we demonstrate an asymptotic model for propagation in the adhesion and viscosity dominated limits by resolving the behaviour of the vapour tip.

This paper is structured as follows. Section II presents the static blister shapes and dynamic model demonstrating the transition from viscosity dominant to adhesion dominant spreading within the thin elastica framework. Section III describes the experimental setup and methods. Finally, the experimental results are analysed and compared with the theoretical model in Sec. IV.

II. THEORETICAL MODEL

To examine the fluid-driven delamination of an adhered elastic sheet (see Fig. 1), a volume of fluid of density ρ and viscosity μ is injected beneath an elastic sheet of thickness d and density ρ_s initially adhered to a horizontal substrate with adhesion energy $\Delta\gamma$. In all dynamic cases the fracture front, R_N, extends beyond the fluid front, R_F, such that a

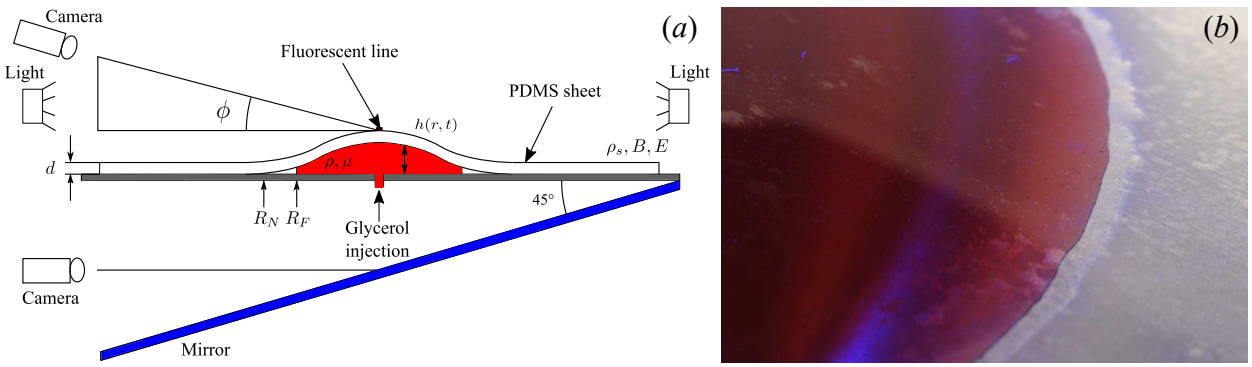

FIG. 1. (a) Schematic diagram of the theoretical model and experimental setup with the physical parameters in the system. (b) Photograph of an experimental fluid front showing lag between fluid front and fracture front.

vapour filled tip exists of length $L = R_N - R_F$. Bending stresses dominate when the vertical deflection of the sheet is smaller than the thickness, $h(r,t) \ll d$. The flow of the fluid is driven by gradients in the reduced pressure $\tilde{p} = p - p_0 - \rho_s g d = B\nabla^4 h + \rho g(h - z)$, where p is the pressure in the fluid, p_0 is a reference pressure and bending stiffness $B = Ed^3/12(1-\nu^2)$, where E and ν are the Young's modulus and Poisson's ratio of the sheet respectively.

For large aspect ratios we may balance viscous drag with the hydrostatic and elastic pressure gradients to describe the deflection of the sheet [2],

$$\frac{\partial h}{\partial t} = \frac{1}{12\mu}\frac{1}{r}\frac{\partial}{\partial r}\left[rh^3\frac{\partial}{\partial r}\left(B\nabla^4 h + \rho g h\right)\right], \tag{2}$$

where global mass conservation gives

$$V(t) = 2\pi\int_0^{R_F} hr\,\mathrm{d}r. \tag{3}$$

The balance between elastic stresses and gravity acting on the fluid gives rise to a natural horizontal, elastogravity lengthscale, $l_{eg} = (B/\rho g)^{1/4}$, and hence characteristic height and time scales may be defined as $H_0 = (12\mu Q/\rho g)^{1/4}$ and $T_0 = H_0 l_{eg}^2/Q$ respectively, where Q is a typical volume flux.

A. Static shapes

Adhesion of the sheet at the perimeter, R_N, allows for the possibility of static solutions with no vapour tip, analogous to the capillary sessile drop [19]. The potential energy of the

blister is balanced by the energy of adhesion between the elastic sheet and the horizontal substrate. For a constant volume V, this gives rise to static shapes with uniform pressure $\tilde{p}$. When the radius is smaller than the elastogravity lengthscale, $R_F \ll l_{eg}$, the pressure within the blister is dominated by bending stresses with $\tilde{p} \simeq B\nabla^4 h$. At the origin the imposition of zero slope and bending moment ensure that the mathematical description of the height of the sheet does not diverge as $r \to 0$. For static shapes the fracture and fluid fronts are concomitant, and continuity with the adjoining flat regions requires that the height and gradient are zero at the front, $h = \nabla h = 0$ at $r = R_F$. The deflection reduces to the classic bell-shaped form [20, 21]

$$h(r) = \frac{\tilde{p}R_F^4}{64B}\left(1 - \frac{r^2}{R_F^2}\right)^2, \tag{4}$$

see Fig. 2 (i) (inset). Global mass conservation (3) and the curvature condition at the front due to adhesion impose $V = \pi\tilde{p}R_F^6/192B$ and $\kappa = \tilde{p}R_F^2/8B$ respectively, where $\kappa = \sqrt{2}/l_{ec}$ [6], and thus determine the radial extent and central deflection,

$$R_F = \left(\frac{24V}{\pi\kappa}\right)^{1/4} \quad \text{and} \quad h_0 = \left(\frac{3\kappa V}{8\pi}\right)^{1/2}. \tag{5}$$

In contrast, for larger volumes when the radius is much greater than the elastogravity lengthscale, $R_F \gg l_{eg}$, gravity becomes important and the uniform pressure contains both elastic and hydrostatic contributions, $\tilde{p} = B\nabla^4 h + \rho g h$. In the interior, the pressure is nearly hydrostatic and hence the height is uniform and the profiles are flat topped. Near the front, on a lengthscale $O(l_{eg})$, the hydrostatic pressure is balanced by elastic stress due to bending the elastic sheet over the periphery. Adhesion at the front therefore imposes curvature, $\kappa \sim h/l_{eg}^2$, which thereby determines the height and radial extent of the static elastic droplet. An analytic solution can be found by matching the interior hydrostatic and edge bending regions with the adhesion condition along the periphery such that the profile

$$h(r) = \kappa l_{eg}^2\left[1 - e^X\left(\cos X - \sin X\right)\right], \tag{6}$$

where $X = (r - R_F)/\sqrt{2}l_{eg}$, see Fig. 2 (ii) (inset). In this sessile elastic limit the radial extent and central deflection are

$$R_F = \left(\frac{V}{\pi\kappa l_{eg}^2}\right)^{1/2} \quad \text{and} \quad h_0 = \kappa l_{eg}^2. \tag{7}$$

Fig. 2 (a, b and c) shows the transition from bending dominant to gravitationally dominant profiles, radial extent and central deflection with increasing volume (blue curves) along with asymptotic scaling from Eqn. 5 and 7 (black dot-dashed lines).

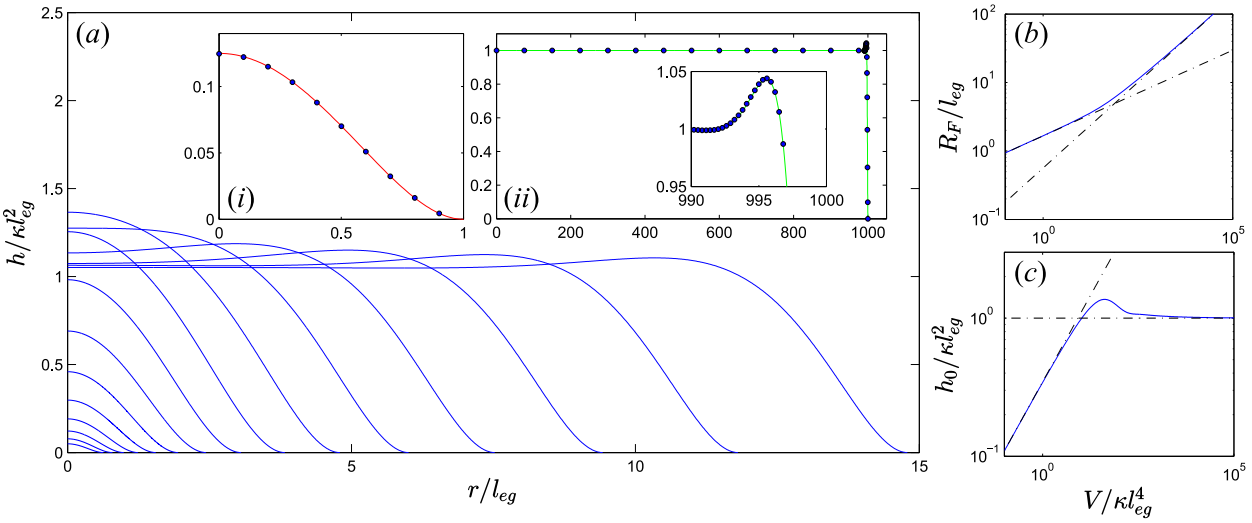

FIG. 2. (a) Plot of the static profiles for a constant volume V transitioning from bending to gravitationally dominated regimes. Inset (i) shows numerical solution in the pure bending regime (blue dots) plotted on top of theoretical profile Eqn. 4 (red curve), and (ii) the numerical solution in the gravity dominant regime with a bending tip (blue dots) plotted on top of theoretical profile Eqn. 6 (green curve). (b) Dimensionless radial extent with volume. (c) Dimensionless central deflection with volume.

These static shapes arise due to the balance between adhesion of the elastic sheet and the substrate at the periphery and the hydrostatic and elastic potential energy of the blister. In Sec. II B we will show that these are the end-member profiles for time dependent spreading due to a constant flux Q, when the rate at which the fluid front advances is slow.

B. Dynamic spreading

In contrast to the static case, dynamic inflation requires the presence of a vapour tip of length $L = R_N - R_F$. This eliminates the inherent divergence of viscous stresses at the fluid front, and thus regularises the flow at the contact line by imposing a finite fluid thickness at the fluid front [12]. An examination of the dominant lengthscales at the tip reveal two possible behaviours when the volume $V(t) = Qt$; either the expansion of the fluid blister is dominated by viscous dissipation, or by the requirement to overcome the energy of adhesion.

At early times, $R_F \ll l_{eg}$, the evolution of the blister is slow, and therefore the interior pressure is nearly constant. The deflection of the sheet in this limit takes the form described

in Eqn. 4. The rate at which the blister expands is determined entirely by processes at the front. Assuming the radial extent of the fluid greatly exceeds the length of the vapour tip, $R_F \gg L$, we can treat the tip as two-dimensional with reduced pressure $\tilde{p}_T = p_T - p_0 - \rho_s g d = Bh^{IV}$, where $\sigma = -\tilde{p}_T$ is large and the tip pressure p_T is negligible compared with the weight of the beam [1, 12]. As in the static case, continuity at the tip requires the height and gradient to be zero $h = h' = 0$ with fracture criterion $h'' = \kappa$ at $r = R_N$. The deflection of the sheet in the vapour tip may then be written as

$$h(r,t) = -\frac{\sigma}{24B}(R_N - r)^3(R_N - r - L) + \frac{h(R_F,t)}{L^3}(R_N - r)^3 - \frac{\kappa}{2L}(R_N - r)^2(R_N - r - L), \tag{8}$$

which extends the vapour tip model ([12] Eqn. (3.5)) to include adhesion at the front.

The rate of advance is determined by matching the interior curvature, $\kappa_{int} = 24Qt/\pi R_F^4$, with that of the front, $h''(R_F, t) = \kappa_F$. Matching the deflection of the sheet and it's first four derivatives at the fluid front we find that the curvature at the front is a combination of that imposed by adhesion and the dynamic curvature from the propagating fluid interface, $\kappa_F \simeq 2h(R_F,t)/L^2 \simeq \kappa + \sigma L^2/8B$. This defines a natural lengthscale $L_C = (B\kappa/\sigma)^{1/2}$ over which the adhesion curvature is felt. A comparison of this lengthscale with the lengthscale of the vapour tip separates viscosity dominant spreading ($L \gg L_C$) from adhesion dominant spreading ($L \ll L_C$).

To determine the spreading rate we look for a travelling wave solution near the tip of the form $h = h_F f[\xi \equiv (r - R_F(t))]$, which satisfies (2),

$$-\dot{R}_F h_F f' = \frac{Bh_F^4}{12\mu}\left(f^3 f^V\right)' \quad \Rightarrow \quad -\dot{R}_F = \frac{Bh_F^3}{12\mu} f^2 f^V, \tag{9}$$

using mass conservation at the fluid front $\dot{R}_F = \lim_{r\to R_F} -h^2 p_r/12\mu$, where $f' = \partial f/\partial\xi$, $f^V = \partial^5 f/\partial\xi^5$. This defines a viscous peeling lengthscale $l_p = (Bh_F^3/12\mu\dot{R}_F)^{1/5}$ [7]. In the viscosity controlled regime, continuity suggests $L \simeq l_p$ at the front along with curvature $\kappa_F \simeq 2h_F/L^2 \simeq \sigma L^2/8B$. The viscous peeling lengthscale is then

$$l_p = \left(\frac{2^{12}(12\mu)B^2\dot{R}_F}{\sigma^3}\right)^{1/7} \tag{10}$$

and demonstrates that spreading is viscosity controlled at early times when $\dot{R}_F$ is large, and hence $l_p \gg L_C$. The front exhibits a dynamic curvature that can be defined without recourse to adhesion [22],

$$\kappa_F \simeq \frac{2h_F}{L^2} \simeq \left(\frac{2^3(12\mu)^2\sigma}{B^3}\right)^{1/7} \dot{R}_F^{2/7}, \tag{11}$$

and it is this curvature which initially controls the propagation. Matching onto the interior curvature κ_{int} thus gives an asymptotic model for the radial extent, central deflection and lag length in the viscosity dominant regime,

$$R_F(t) = 1.52 \left(\frac{Q^7B^3}{(12\mu)^2\sigma}\right)^{1/30} t^{3/10}, \tag{12}$$

$$h_0(t) = 0.41 \left(\frac{(12\mu)^2\sigma Q^8}{B^3}\right)^{1/15} t^{2/5}, \tag{13}$$

$$L(t) = 1.19 \left(\frac{(12\mu)^4B^9Q}{\sigma^{13}}\right)^{1/30} t^{-1/10}, \tag{14}$$

(see the Supplemental Material [23]). We emphasise that these initial solutions are independent of the adhesion at the front.

At later times, $t > (12\mu)^{4/3}Q^{1/3}\sigma^{2/3}/B^2\kappa^5$, the decrease in $\dot{R}_F$ implies that $l_p \ll L_C$, and there is therefore a transition to adhesion control where the peeling lengthscale is no longer important at the tip. The curvature at the front is predominantly that imposed by adhesion, $\kappa_F \simeq \kappa$. Thus, when adhesion at the front becomes dominant, the blister transitions through a series of quasi-static solutions, identical to those described by (5), now with $V = Qt$,

$$R_F(t) = \left(\frac{24Q}{\pi\kappa}\right)^{1/4} t^{1/4}, \tag{15}$$

$$h_0(t) = \left(\frac{3\kappa Q}{8\pi}\right)^{1/2} t^{1/2}. \tag{16}$$

Importantly, these late time solutions are now independent of the fluid viscosity, as well as the presence of a vapour tip.

The lag length L is determined by considering mass conservation at the fluid front, $\dot{R}_F \simeq h_F^2\sigma/12\mu L$, where there is a jump in pressure of $O(\sigma)$ at the fluid-vapour interface, and the curvature due to adhesion, $2h_F/L^2 \simeq \kappa$. Hence the lag length is determined by the flow of a viscous fluid slowly infilling a wedge whose geometry is determined by adhesion,

$$L(t) = 0.82 \left(\frac{(12\mu)^4Q}{\sigma^4\kappa^9}\right)^{1/12} t^{-1/4}. \tag{17}$$

It can be shown that the assumptions of constant interior pressure and pure bending ($r \ll l_{eg}$ and $h \ll d$) are valid provided $(12\mu B/Q\sigma^2)^{1/2} \ll t \ll l_{eg}^4\kappa/Q,\, d^2/Q\kappa$ by substituting the scalings for the two regimes into the original time evolution equation for the

deflection (2). For axisymmetric spreading the transition from viscosity dominant to adhesion dominant spreading occurs at transitional horizontal, height and time scales $R_C = (12\mu Q)^{1/3}\sigma^{1/6}/B^{1/2}\kappa^{3/2}$, $H_C = (12\mu Q)^{2/3}\sigma^{1/3}/B^{7/15}\kappa^2$, and $T_C = (12\mu)^{4/3}Q^{1/3}\sigma^{2/3}/B^2\kappa^5$, respectively.

Dynamic spreading of a fluid beneath an elastic sheet is governed by a competition between viscous dissipation and the energy required to overcome adhesion. At early times, the spreading is viscosity dominant, controlled by the pressure gradients driving fluid into the tip, and given by the no-adhesion solution, [12]. When $l_p \ll L_C$, there is a transition to adhesion control, where the lag length no longer plays a role in the propagation of the fracture front. Instead the spreading tends towards the static case controlled by the energy of adhesion at the tip and is independent of viscosity of the fluid and pressure in the vapour tip. The regimes described here have parallels with those described for a semi-infinite hydraulic fracture evolving from a viscosity dominant to a toughness dominant crack in an elastic half-space [13], and, as shown in the following section, can be readily observed in experiments on thin elastica.

III. EXPERIMENTAL METHODS

Experiments conducted to investigate the fluid-driven fracturing of adhered elastica consisted of injecting a viscous fluid beneath an elastic sheet adhered to a horizontal substrate (see Fig. 1). An elastic sheet of polydimethylsiloxane (PDMS) was used with diameter $917 \pm 1\,\text{mm}$ and thickness $d = 9.8 \pm 0.3\text{mm}$. The bending stiffness $B = 0.18 \pm 0.02\,\text{Pa.m}^3$ was measured using loop [24] and circular blister tests [25]. The PDMS sheet was adhered to a horizontal glass table using TUFFBond$^{\text{TM}}$ Adhesive Mount Film of thickness $0.15 \pm 0.01\,\text{mm}$. Glycerine-water solutions were injected between the glass table and composite PDMS and adhesive sheet. Injection was through a 5.5 mm diameter aperture and the flux was determined by measuring the volume injected on the table from the deflection profiles.

The deformation of the PDMS sheet was measured by imaging a fluorescent line on top of the sheet at a known oblique angle ϕ, as shown in Fig 1. To improve the contrast between the line and the background, the line was illuminated by a blue light and the blue colour channel was isolated in the digital images acquired. A filtered image taken using this

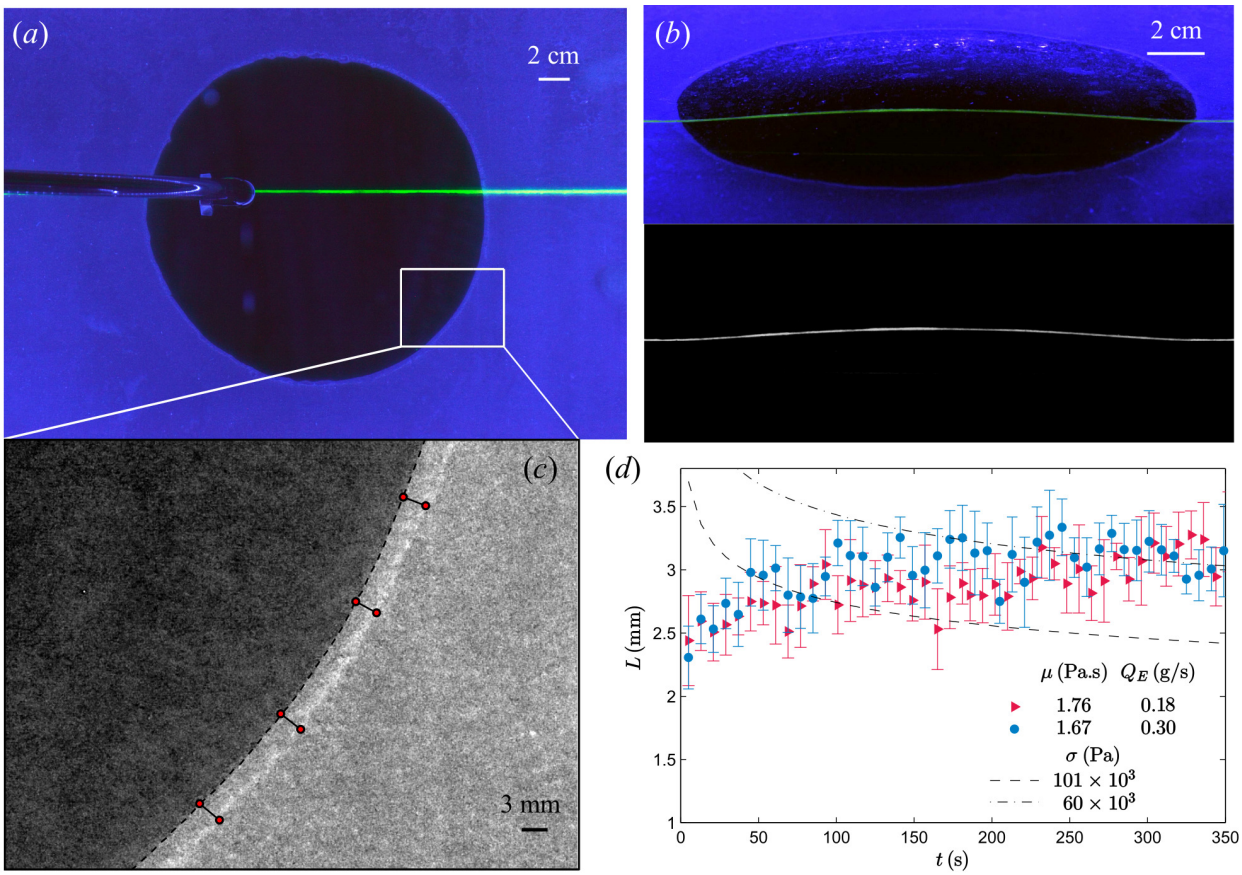

FIG. 3. (a) Sample image taken underneath experimental blister. (b) Sample image taken of fluorescent line on top of PDMS sheet and filtered image showing the deflected line. (c) Zoom in of the edge of the blister filtered to show intensity contrast between vapour tip and the substrate. Fluid front given by the black-dashed line with lag lengths given by pairs of red dots. (d) Lag length with time for two experiments in the viscosity dominant regime.

method is shown in Fig. 3(b) demonstrating the contrast achieved. Deflections of the line are determined by comparing with a reference image of the undeformed PDMS taken prior to injection. A Gaussian was then fit to the intensity profile at each vertical strip of pixels where the central peak was chosen as the centreline. To reduce scatter, an average was taken every 10 pixels. The final profile for this sample snapshot is plotted in Fig. 4 for $t = 64$ s, $\mu = 2.12$ Pa.s and $Q_E = 0.39$ g/s.

The fluid and fracture fronts were measured by imaging from underneath the glass substrate using a mirror placed at 45° to the base (see Figs. 1, 3(a)). A high contrast between the fluid and the substrate meant the fluid front could be automatically detected, as

demonstrated in Fig. 3(c) by the black-dashed line. Due to the small, non-axisymmetric deviations, a circle was fit to the points detected at the fluid front to give radial extent R_F at each timestep.

Partial internal reflection within the vapour tip allowed for distinction between the fluid front and fracture front. This is demonstrated in Fig. 3(c) where the blue colour channel is isolated and the contrast increased. The scatter in the brightness of the vapour tip meant the fracture front could not be automatically chosen. As a result, the fracture front was manually chosen at 10 points around the edge of the blister. The red dots in Fig. 3(c) show the automatically chosen R_F and manually picked R_N. The lag length is determined at each pair of points and an average is taken for each timestep. The results of this procedure are shown in Fig. 3(d), with the error estimated from the standard deviation of the 10 points measured at each timestep.

IV. RESULTS AND DISCUSSION

A. Viscosity dominant spreading

A series of constant flux injection experiments were carried out in the viscosity dominant and adhesion dominant regimes. In the viscosity dominant regime, pure glycerine was used with viscosities $\mu = 1.67 - 2.12 \pm 0.02$ Pa.s and injected at mass fluxes of $Q_E = 0.18 - 0.39 \pm 0.005$ g/s. Fig. 4 shows the measured deflection for an experiment with mass flux $Q_E = 0.39$ g/s and viscosity $\mu = 2.12$ Pa.s for $t = 64$-130 s, with profiles plotted every $\Delta t = 6$ s. From Sec. II, Eqns. 12 and 13 describe the radius and central deflection at time t in the viscosity dominant regime. By scaling the radius and height of the profiles in Fig. 4(a) by these expressions for R_F and h_0, the profiles collapse on to a universal curve described by (4), see Fig. 4(b). The black-dashed line shows the theoretical profile Eqn. 4 demonstrating excellent agreement with the collapsed dataset. This confirms that in the dynamic spreading case the shape of the blister remains unchanged from the classic bell-shaped profile.

Because the pressure within the central blister was quasi-static, the position of the blister with respect to the injection hole was only weakly constrained and hence was very sensitive to initial experimental conditions. For example, the differing angle the injection pipe made to the horizontal substrate, or differences in the adhesion energy in the immediate vicinity

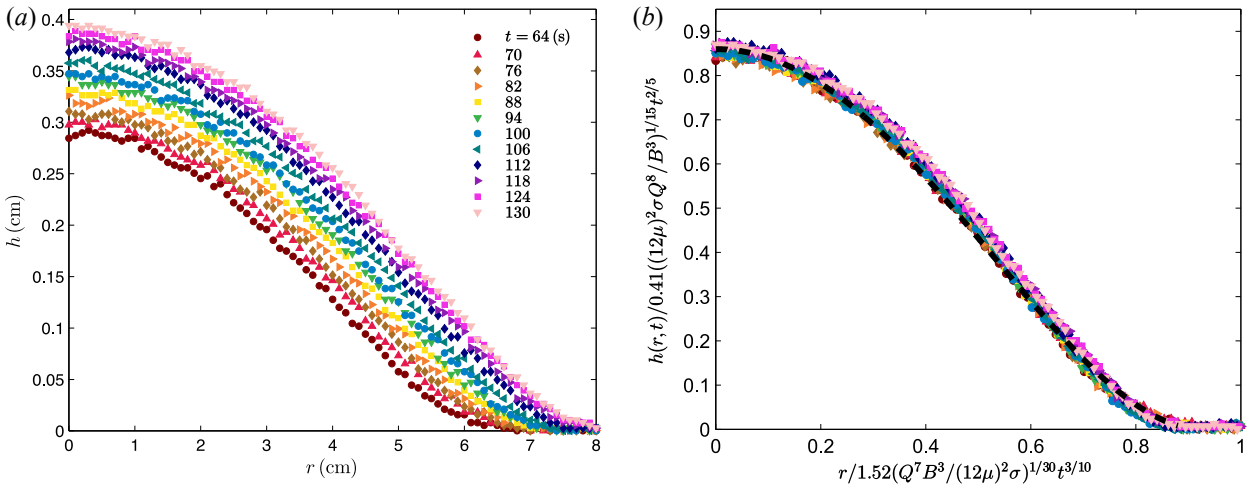

FIG. 4. Deflection profiles for an experiment in the viscosity dominant regime with mass flux $Q_E =$ 0.39 g/s, viscosity $\mu = 2.12$ Pa.s, $\sigma = 101 \times 10^3$ Pa for $t =$ 64-130 s, where $\Delta t = 6$ s. (a) Measured deflection, and (b) deflection scaled with theoretical expressions (12, 13). The black-dashed line shows the theoretical profile (4).

of the injection hole resulted in migration of the blister off-centre, see Fig. 3(a). At the start of each experiment, the fluorescent line on the PDMS sheet was aligned with the injection hole, and hence for the same experiments the detected deflection profile is of a chord taken off-centre. For these reasons, the magnitude measured radius and height in Fig. 4(a) are less than the theoretical prediction for a profile through the origin, i.e. the dimensionless radial extent and central deflection in Fig. 4(b) are less than 1. However, as these measurements are of a chord of the symmetric bell-shaped profile, they show excellent collapse and confirm the predicted deflection shape. In the next paragraph we will show that the position of the blister relative to the injection hole has no impact on the dynamics of propagation. This supports the assumption that the interior of the blister remains quasi-static with constant reduced pressure $\tilde{p}$.

Fig. 5(a) shows the radial extent with time for six experiments with different mass fluxes in the viscosity dominant regime. In Fig. 5(b) the radial extent is scaled with $(Q^7B^3/((12\mu)^2\sigma))^{1/30}$ from Eqn. 12. (Here we have taken $\sigma = 101 \times 10^3$ Pa which we will justify when describing the measured lag length). This collapses the experiments onto to one curve with power law exponent 3/10. Hence, the experimental data is in good agreement with the theoretical scaling $R_F \sim t^{3/10}$ in the viscosity dominant regime. This also

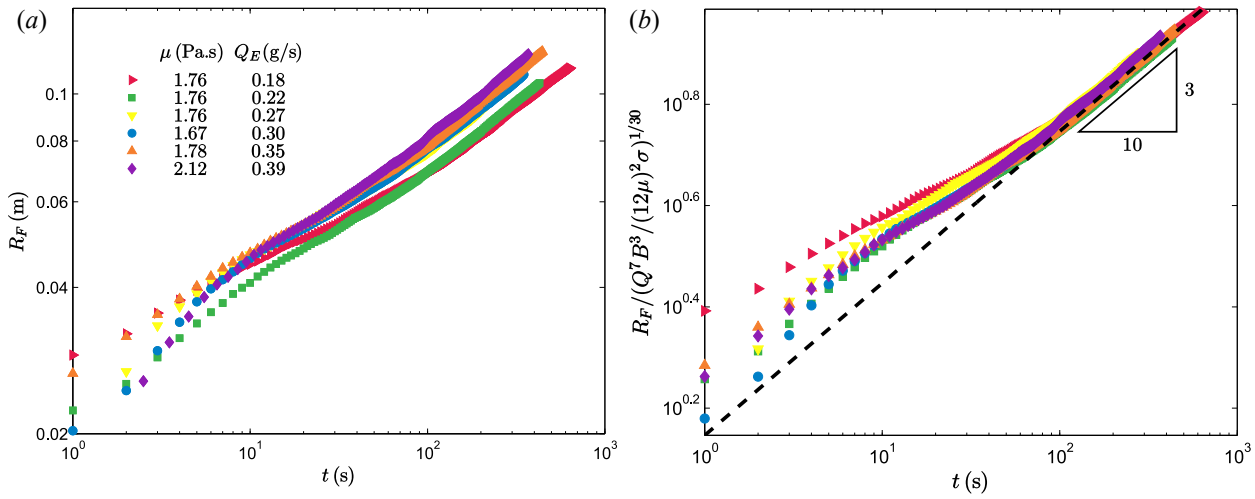

FIG. 5. Radial extent with time in the viscosity dominant regime. (a) Measured radial extent. (b) Radial extent scaled with $(Q^7B^3/((12\mu)^2))^{1/30}$. Black-dashed line corresponds to best fit $R_F/(Q^7B^3/((12\mu)^2\sigma))^{1/30} = 1.40\,t^{3/10}$.

highlights the position of the blister with respect to the injection hole has no impact on the dynamics of propagation. The black-dashed line in Fig. 5(b) corresponds to the best fit line $R_F/(Q^7B^3/((12\mu)^2\sigma))^{1/30} = 1.40\,t^{3/10}$, where the prefactor is within 8% of the theoretical prefactor 1.52.

For the viscosity dominant regime, we manually measured the lag length using the methods described in Sec. III, see Fig. 3(c). Fig. 3(d) plots the lag length for two experiments with mass fluxes Q_E =0.18, 0.30 g/s, where L is the average of the measured lag lengths and the error bars are one standard deviation above and below the mean. The overlapping error bars for the two experiments suggest there is no measurable difference between the lag lengths which is supported by the negligible dependence on the volume flux, $Q^{1/30}$, in Eqn. 14. The black dashed and dot-dashed lines in Fig. 3(d) are Eqn. 14 plotted with $\sigma = 101 \times 10^3$, 60×10^3 Pa respectively. If the vapour tip produces a near vacuum pressure at the front the vapour tip pressure would be zero $p_T = 0$ and hence $\sigma = p_0 + \rho_s g d - p_T \simeq 101 \times 10^3$ Pa. The magnitude of the lag length observed suggests the tip pressure is non-negligible, which can be explained by considering the experimental setup. Some small amount of air may have been trapped when placing the adhesive sheet onto the glass substrate. These bubbles may act to increase the pressure at the tip and hence explain the smaller value of σ required to fit the lag length observed.

The measured lag length also appears to be smaller at early times, in contrast to our theoretical prediction. However, it should be noted that Eqn. 8 has been written in the limit $R_F \gg L$, which may be violated at early times. As a result, when fluid is first injected the elastic sheet is clamped at the radius of the injection hole, and the sheet is lifted up by the injection of fluid with a small lag length at the front. As the blister first begins to propagate beyond this radius the lag length first begins to increase as it relaxes to the dynamically determined extent. This transient behaviour can be seen in Fig. 5(b) where the radial extent does not collapse at early times and in Fig. 3 where the lag length increases initially, and continues until the pressure decreases to that given by the elastic pressure i.e. until the blister is large enough that the initial pressure build up is negligible. The constant lag length observed at late time during the viscosity dominant spreading is then consistent with the slowly varying lag length $L \sim t^{-1/10}$ predicted by the theoretical model.

B. Adhesion dominant spreading

In the adhesion dominant regime, glycerine-water solutions were used with viscosities $\mu = 0.03 - 0.17 \pm 0.005\,\mathrm{Pa.s}$ injected at mass fluxes $Q_E = 0.18 - 0.58 \pm 0.005\,\mathrm{g/s}$. Fig. 6(a) shows the measured radial extent with time. Under the assumption that the adhesion energy is constant, we scale the radial extent by $Q^{1/4}$ from Eqn. 15 and find that the prefactor c, where $R_F = c(Qt)^{1/4}$, is dependent on the glycerol-water content of the injected fluid. From Eqn. 15, c is a constant set by the curvature imposed by adhesion at the front. Hence, we find that the curvature at the front, which is constant for any given experiment, varies with the fluid viscosity; and hence is a function of the glycerol-water content, and that blistering is therefore a sensitive measure of the rheology of the adhesive tape. We independently measure the curvature κ for each experiment by fitting a quadratic to the tip region of the detected deflection profiles. Fig. 6(c) (inset) plots the measured curvature κ against the prefactor c for the six experiments (see the Supplemental Material [23]). We find that $c = c(\kappa)$ where $c = 1.45\,\kappa^{-1/4}$, black-dashed line, where the exponent of κ agrees with the static scaling given by Eqn. 15. In Fig. 6(b) the radial extent is scaled by $(Q/\kappa)^{1/4}$ using the measured values of κ which shows an excellent collapse of the experimental data onto one curve with power law exponent 1/4, where the black-dashed line is best fit $R_F/(Q/\kappa)^{1/4} = 1.45\,t^{1/4}$, where the prefactor is within 13% of theoretical prefactor 1.66. This discrepancy is largely due to the

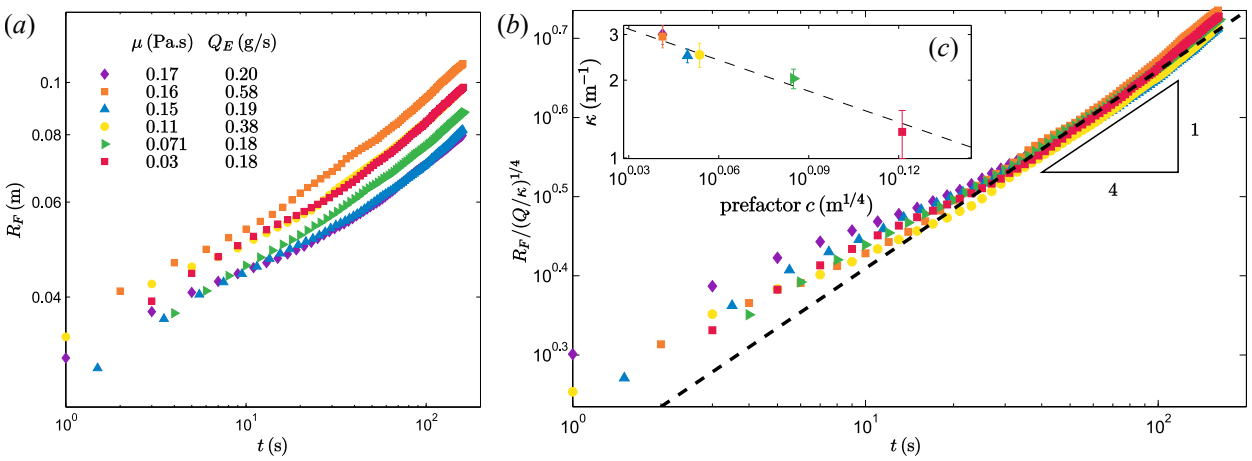

FIG. 6. Radial extent with time in the adhesion dominant regime. (a) Measured radial extent. (b) (inset) Measured curvature κ plotted against measured prefactor c, where $R_F = c(Qt)^{1/4}$. Black-dashed line given by $c = 1.45\,\kappa^{-1/4}$. (c) Radial extent scaled with $(Q/\kappa)^{1/4}$. Black-dashed line corresponds to best fit $R_F/(Q/\kappa)^{1/4} = 1.45\,t^{1/4}$.

inherent limitations in the measurement of experimental curvature κ. We hypothesise that the decrease in curvature (and hence decrease in adhesion energy $\Delta\gamma$) with viscosity can be explained by a chemical interaction between the fluid and adhesive material when the lag length becomes small which weakens the adhesive strength, and hence reduces curvature.

Unlike in the viscosity dominant regime, in the adhesion dominant regime no measurable lag region was observed during experiments, however condensation droplets were seen when pulling off the adhesive tape. This suggests that the vapour tip was present and at low enough pressures to exsolve gas from the glycerine-water mix but was of sufficiently small scale such that it could not be distinguished from the fluid front during experiments using our optical technique. Substituting the experimental parameters μ, Q and κ, and taking $\sigma = 101 \times 10^3$ Pa, into the expression for the lag length in the adhesion dominant regime Eqn. 17 gives $L \simeq 0.8 - 1.2 \times 10^{-}3$ m. This is consistent with a lag length which was below the image resolution as demonstrated in Fig. 3.

C. Transition timescales

The measured curvature values in the adhesion dominant regime provide a lower bound on the absolute adhesive strength without interaction with the glycerine-water solution,

$\kappa_{min} = 3.04\,\mathrm{m}^{-1}$, $\Delta\gamma_{min} = 0.83\,\mathrm{Jm}^{-2}$, and an estimate of the magnitude of the dynamic curvature in the viscosity dominant regime, given by (11), from the profile seen in Fig. 4, gives an upper bound, $\kappa_{max} = 3.19\,\mathrm{m}^{-1}$, $\Delta\gamma_{max} = 0.92\,\mathrm{Jm}^{-2}$. These adhesion energies are comparable to values previously obtained [18]. We can therefore estimate the transition timescale between the viscosity and adhesion dominant regimes. For the pure glycerine experiments we estimate $t_C = 1.95T_C \simeq 153 - 253\,\mathrm{s}$ however we do not anticipate seeing adhesion dominant spreading due to the transition to gravity control. For the glycerine-water solutions, using the measured values of curvature, we estimate the transition timescale to be $t_C = 1.95T_C \simeq 9 - 32\,\mathrm{s}$. Both of these transition timescales are in agreement with the timescales over which the experimental data collapse in the viscosity and adhesion dominant regimes, see Figs. 5, 6.

V. DISCUSSION

Static blister tests have long been used as a measure of the strength of adhesion between two materials [6, 26]. The coupling of viscous fluid delaminating adhered elastica has moved concentration towards the study of blister dynamics [7, 12] with application in a wide range of biological and industrial settings. These include the flow of biofluids through deformable vessels [8] such as the reopening of the pulmonary airways [27]; and the manufacturing of stretchable electronics [5] made from buckled film on an elastomeric substrate [28]. The experiments described in Sec. IV have highlighted that blister dynamics could again usefully be applied to understanding the strength of adhesion with blistering providing a sensitive measure of the rheology of adhesive tape. In addition, the treatment of using thin elastica coupled with an adhesive sheet has provided a simple, new approach to understanding fluid-driven fracturing in an experimental setting. Hence, this experimental setup could lend itself to investigating other outstanding problems such as the effect of inhomogeneity in adhesive strength on the dynamics of fluid-driven fractures.

In Sec. II we described the static shapes for a given volume V and the dynamic spreading regimes for a constant flux injection, $V = Qt$. One can think of connecting these two cases by considering the evolution of a blister once injection has stopped. For a blister propagating in the viscosity dominant regime, there would be a transition to adhesion control at the front as the front velocity slows down, with a transient behaviour as the blister adjusts to the static

shape. Conversely, for spreading in the adhesion dominant regime, the blister progresses through a series of quasi-static shapes. Hence, if injection is stopped the fracture front would remain stationary while the deceleration of the fluid front would be accomodated by infilling of the vapour tip. This extension could easily be tested in our experimental setup with the ability to track the evolution of the fluid and fracture fronts as described in Sec. III.

VI. CONCLUSION

Our theoretical model describes fluid-driven fracturing of adhered elastica by the introduction of a vapour tip separating the fracture and fluid fronts. Coupled with a fracture criterion imposed at the front, this leads to the possibility of static shapes where the potential energy of the blister balances the energy required for fracture. For dynamic inflation, spreading can be split into two distinct regimes: viscosity dominant spreading controlled by the pressure gradient driving fluid into the vapour tip, and adhesion dominant spreading controlled by interfacial adhesion. Experiments using thin elastica adhered to a horizontal substrate have yielded excellent comparisons with the theoretical model and demonstrated spreading behaviour in the two regimes. The experimental techniques developed have also provided further concrete evidence for the formation of an experimental vapour tip consistent with that predicted by the theoretical model. The fluid lag has previously been observed in laboratory experiments on the fracturing of elastic blocks [15–17], however our study is the first to link an analytical prediction for the lag length with an experimental analogue. This study gives further insight into the processes involved in fluid-driven fracturing and provides an experimental framework to investigate fluid-driven fracturing of elastic media more generally.

[1] E. Detournay, "Mechanics of Hydraulic Fractures," Annu. Rev. Fluid Mech **48**, 311–339 (2016).

[2] C. Michaut, "Dynamics of magmatic intrusions in the upper crust: Theory and applications to laccoliths on Earth and the Moon," J. Geophys. Res. **116**, 1–19 (2011).

[3] A. M. Rubin, "Propagation of Magma-Filled Cracks," Annu. Rev. Earth Planet. Sci **23**, 287–336 (1995).

[4] V. C. Tsai and J. R. Rice, "A model for turbulent hydraulic fracture and application to crack propagation at glacier beds," J. Geophys. Res. Earth Surf. **115**, 1–18 (2010).

[5] Y. Sun, W. M. Choi, H. Jiang, Y. Y. Huang, and J. A. Rogers, "Controlled buckling of semiconductor nanoribbons for stretchable electronics." Nat. Nanotechnol. **1**, 201–7 (2006).

[6] T. J. W. Wagner and D. Vella, "Floating Carpets and the Delamination of Elastic Sheets," Phys. Rev. Lett. **107**, 1–4 (2011).

[7] J. R. Lister, G. G. Peng, and J. A. Neufeld, "Viscous Control of Peeling an Elastic Sheet by Bending and Pulling," Phys. Rev. Lett. **111**, 1–5 (2013).

[8] J. B. Grotberg and O. E. Jensen, "Biofluid Mechanics in Flexible Tubes," Annu. Rev. Fluid Mech **36**, 121–47 (2004).

[9] D. Pihler-Puzović, P. Illien, M. Heil, and A. Juel, "Suppression of Complex Fingerlike Patterns at the Interface between Air and a Viscous Fluid by Elastic Membranes," Phys. Rev. Lett. **108**, 1–5 (2012).

[10] C. Huh and L. E. Scriven, "Hydrodynamic model of steady movement of a solid/liquid/fluid contact line," J. Colloid. Interf. Sci. **35**, 85–101 (1971).

[11] M. H. Eres, L. W. Schwartz, and R. V. Roy, "Fingering phenomena for driven coating films," Phys. Fluids **12**, 1278 (2000).

[12] I. J. Hewitt, N. J. Balmforth, and J. R. De Bruyn, "Elastic-plated gravity currents," Eur. J. Appl. Math. **26**, 1–31 (2015).

[13] D. I. Garagash and E. Detournay, "The Tip Region of a Fluid-Driven Fracture in an Elastic Medium," J. Appl. Mech. **67**, 183–192 (1999).

[14] J. R. Lister, "Buoyancy-driven fluid fracture: the effects of material toughness and of low-viscosity precursors," J. Fluid Mech. **210**, 263–280 (1990).

[15] W.L. Medlin and L. Masse, "Laboratory Experiments in Fracture Propagation," Soc. Pet. Eng. J. **24**, 256–268 (1984).

[16] A. P. Bunger, E. Detournay, and R. G. Jeffrey, "Crack tip behavior in near-surface fluid-driven fracture experiments," C. R. Mécanique **333**, 299–304 (2005).

[17] A. P. Bunger, E. Gordeliy, and E. Detournay, "Comparison between laboratory experiments and coupled simulations of saucer-shaped hydraulic fractures in homogeneous brittle-elastic solids," J. Mech. Phys. Solids **61**, 1636–1654 (2013).

[18] T. J. W. Wagner and D. Vella, "The Sticky Elastica': delamination blisters beyond small deformations," Soft Matter **9**, 1025–1030 (2013).

[19] L. H. Tanner, "The spreading of silicone oil drops on horizontal surfaces," J. Phys. D. Appl. Phys. **12**, 1473–1484 (1979).

[20] S. Timoshenko and S. Woinowsky-Krieger, *Theory of Plates and Shells* (1959).

[21] D. Pollard and A. Johnson, "Mechanics of growth of some laccolithic intrusions in the Henry Moutains, Utah, II. Bending and failure of the overburden layers and sill formation," Tectonophysics **18**, 311–354 (1973).

[22] J. C. Flitton and J. R. King, "Moving-boundary and fixed-domain problems for a sixth-order thin-film equation," Eur. J. Appl. Math. **15**, 713–754 (2004).

[23] See Supplemental Material at [URL will be inserted by publisher] for discussion of the travelling wave solution and numerical analysis of Eqn. (9), and for measurements of the front curvature κ in experiments in the adhesion dominant regime.

[24] I. M. Stuart, "A loop test for bending length and rigidity," Brit. J. Appl. Phys. **17** (1966).

[25] B. M. Malyshev and R. L. Salganik, "The strength of adhesive joints using the theory of cracks," Int. J. Fract. Mech. **1**, 114–128 (1965).

[26] H. M. Jensen, "The blister test for interface toughness measurement," Eng. Fract. Mech. **40**, 475–486 (1991).

[27] M. Heil and A. L. Hazel, "Fluid-Structure Interaction in Internal Physiological Flows," Annu. Rev. Fluid Mech. **43**, 141–162 (2011).

[28] D. Y. Khang, J. A. Rogers, and H. H. Lee, "Mechanical buckling: Mechanics, metrology, and stretchable electronics," Adv. Funct. Mater. **19**, 1526–1536 (2009).